On the Feasibility of Hijacking MLLMs' Decision Chain via One Perturbation

Changyue Li¹, Jiaying Li¹, Youliang Yuan¹, Jiaming He², Zhicong Huang³, Pinjia He¹*

The Chinese University of Hong Kong, Shenzhen

University of Electronic Science and Technology of China, ³ Ant Group

Abstract

Conventional adversarial attacks focus on manipulating a single decision of neural networks. However, real-world models often operate in a sequence of decisions, where an isolated mistake can be easily corrected, but cascading errors can lead to severe risks.

This paper reveals a novel threat: a single perturbation can hijack the whole decision chain. We demonstrate the feasibility of manipulating a model's outputs toward multiple, predefined outcomes, such as simultaneously misclassifying "non-motorized lane" signs as "motorized lane" and "pedestrian" as "plastic bag".

To expose this threat, we introduce Semantic-Aware Universal Perturbations (SAUPs), which induce varied outcomes based on the semantics of the inputs. We overcome optimization challenges by developing an effective algorithm, which searches for perturbations in normalized space with a semantic separation strategy. To evaluate the practical threat of SAUPs, we present RIST, a new realworld image dataset with fine-grained semantic annotations. Extensive experiments on three multimodal large language models demonstrate their vulnerability, achieving a 70% attack success rate when controlling five distinct targets using just an adversarial frame.

1. Introduction

Visual multimodal large language models (MLLMs) like Llava [22], Qwen-VL [2], GPT-4V [1], and Gemini [8] are susceptible to adversarial perturbations [15, 28], where image hijacks [4] enable precise control over models' outputs, posing a significant threat to downstream content.

In real-world applications like autonomous driving [38] and robotic tasks [18], continuous image frames are constantly captured and fed into the MLLM for a sequence of decisions (i.e., decision chain). In such applications, an isolated mistake can be easily corrected, but cascading errors can lead to severe risks. However, current research on uni-



Figure 1. Illustration of hijacking of the MLLM's decision chain. The adversary pastes the perturbation onto the camera. Once the vehicle starts and perceives images, the MLLM accurately outputs the attacker's predefined target content based on the image semantics, cumulatively guiding the vehicle to a predefined destination.

versal adversarial perturbations (UAPs) [26, 27] overlooks the need to mislead the model's decision chain. Existing studies on MLLM even struggle to achieve universal image hijacking; they either construct perturbations per image [4, 24] or manipulate both images and prompts [12, 23].

This paper aims to reveal a novel threat: the adversary can hijack the model's decision chain via one perturbation. As illustrated in Figure 1, with this capability, the adversary only needs to generate and paste a noise frame before the car starts. When perceiving perturbed images, the system will accurately output the attacker's predefined target content based on the image semantics, which cumulatively guides the vehicle to a predefined destination.

We refer to such perturbations as Semantic-Aware Universal Perturbations (SAUPs) due to their unique semantic-aware ability: they can "actively" sense the input image's semantics and map it to a predefined label. SAUPs also maintain the universality property, enabling the perturbation to generalize across unseen inputs.

Searching for SAUPs presents new optimization challenges: supporting multiple distinct targets constrains the feasible solution space, and interference among targets leads to misalignment with the semantics. To overcome optimization challenges, we propose the Semantic-ORiented aTtack (SORT), which comprises two key components: normalized space optimization and semantic separation optimization. (1) Instead of using the raw pixel space like previous work, we leverage the space after image normal-

^{*}Pinjia He is the corresponding author.

ization as a stable foundation for optimization. (2) To address the obfuscation between predefined targets, we combine cross-entropy loss and margin loss.

For a comprehensive understanding of the semantic-aware ability of SAUPs, we not only use the existing image classification dataset (i.e., ImageNet [9]), but also annotate a new dataset called **Real Image Sequence Trajectories** (RIST). RIST contains more than 1,000 real-world images and comprises 28 distinct image trajectories, sourced from established autonomous driving [38] and robotic manipulation [25] datasets. RIST captures diverse vehicular navigation and indoor robotic tasks across varied environmental conditions, covering rich content.

Extensive experiments are conducted on three MLLMs, Llava1.5, Qwen2.5-VL, and InternVL3, leveraging the ImageNet and RIST datasets to investigate performance across various semantic granularities. The results show that SAUPs easily hijack both models under various settings. For example, one perturbation is sufficient to mislead Qwen, achieving success rates of 93%, 77%, 61%, and 66% under 2, 3, 4, and 5 targets, respectively.

Our further analysis reveals that the effectiveness of SAUPs primarily lies in aligning image semantic directions with distinct target labels. We demonstrate that incorporating optimization in the normalized space is crucial for generating effective SAUPs, while employing semantic separation optimization can further enhance performance. ¹

We summarize the main contributions as follows:

- We reveal a novel threat that a perturbation can precisely hijack the MLLM's decision chain, and analyze the perturbed image features in the latent space.
- We propose SORT, an effective algorithm to find such perturbations, and introduce RIST, a dataset with finegrained semantic annotations.
- We conduct extensive experiments to analyze the vulnerability of MLLMs to SAUPs across three representative models, achieving a 66% attack success rate over five targets using a single frame against Qwen.

2. Related Work

2.1. Adversarial Perturbations

Adversarial perturbations have been demonstrated [14, 32] that subtle perturbations added to input data could significantly alter model predictions. A pivotal advancement is the discovery of UAP [26, 36], which are input-agnostic perturbations effective across diverse samples.

However, current adversarial perturbation methods primarily focus on manipulating a single decision of neural networks, either causing misclassification (i.e., nontargeted attacks [6]) or steering toward a predefined target label (i.e., targeted attacks [27]). Real-world AI systems,

such as autonomous driving or the embodied AI [18], often rely on sequential decision-making processes. This reduces the practical threat of existing attacks, as they cannot simultaneously mislead an entire decision chain.

2.2. Vulnerability of MLLMs

The rapid development of MLLMs [2, 22] has raised new security concerns. Recent studies [28, 30, 39, 40] reveal that MLLMs inherit the vulnerability to adversarial perturbations. According to the degree of control over the attack, existing methods can be categorized into two types: semantic misleading and image hijacking.

Semantic misleading [21, 37, 41] only requires the model to misunderstand the meaning of the image. They typically deceive the vision encoder of MLLMs, causing it to provide incorrect image representations to the downstream language model, and consequently leading to incorrect outcomes in subsequent visual tasks.

In contrast, image hijacking [4, 23, 24] aims for precise control over the model's outputs. They often employ end-to-end optimization. Due to their objective to fully dictate the output, such attacks pose a greater threat. For example, attackers can induce the model to generate specific bash commands, or bypass rule checks in downstream tasks [4].

2.3. Distinction from Prior Work

Some previous studies have explored similar properties of adversarial perturbations, but they significantly differ from this paper. C-PGC [12] proposes a UAP against vision-language models, which requires manipulating both image and text modalities, and consequently, it cannot achieve image hijacks or attack the decision chain. MultiAttack [13] shows that a single perturbation can map various inputs to targets. However, this perturbation is not universal, being effective only within the training set and failing to expose the semantic-aware capability.

3. Methodology

3.1. Problem Statement

Consider the MLLM as a function $f: \mathcal{V} \times \mathcal{T} \to \mathcal{Y}$, which maps an image $\mathbf{x} \in \mathcal{V}$ and a prompt $\mathbf{p} \in \mathcal{T}$ to a logit output $\mathbf{y} \in \mathcal{Y}$. The output \mathbf{y} typically consists of a sequence of token logits produced autoregressively.

Our goal is to obtain a single adversarial perturbation $\delta \in \mathcal{V}$, that can be applied to any image $\mathbf{x}^{(c)}$ from the semantic clustering $c \in \{1, 2, \dots, C\}$, causing the model to generate a predefined, class-specific target $\mathbf{t}^{(c)} = t_{1:N}^{(c)}$.

We refer to this type of perturbation as *semantic-aware universal perturbations*, characterized by its ability to induce different targets depending on the input semantics.

The workflow for SAUPs is illustrated in Figure 2. Formally, given a dataset \mathcal{D} where each item consists of triples

¹The code will be released upon the acceptance of this paper.

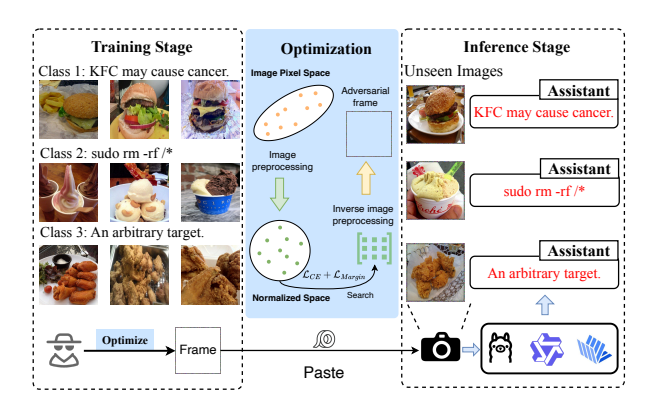


Figure 2. Illustration of SAUPs' workflow. The adversary first collects images from several classes and assigns a specific target label to each class. These images are then used to train the adversarial perturbation (e.g., an adversarial frame). Once trained, the perturbation can be applied to other unseen images, causing MLLMs to generate the exact target sentences conditioned on the semantic content of the input image.

 $\{\mathbf{p}, \mathbf{x}^{(c)}, \mathbf{t}^{(c)}\}\$, the SAUP is obtained by solving the following optimization problem:

$$\arg\min_{\delta} \mathbb{E}_{\mathcal{D}} \left\{ \mathcal{L} \left(f \left(\mathcal{A}(\mathbf{x}^{(c)}, \delta), \mathbf{p} \right), \mathbf{t}^{(c)} \right) \right\}$$
 (1)

where \mathcal{L} is a loss function (details in Section 3.3), $\mathcal{A}(\cdot, \cdot)$ represents the perturbation append operation.

$$\mathcal{A}(\mathbf{x}, \delta) = \left[\mathbf{x} \cdot (\mathbf{1} - \mathbf{r}) + \delta \cdot \mathbf{r}\right]_{\mathbf{0}}^{\mathbf{1}}$$
 (2)

where $[\cdot]_a^b = \min{(\max{(\cdot,a)},b)}$, and \mathbf{r} masks the allowable region where the perturbation can be applied.

Semantic Granularity and Real-World Dataset. Since SAUPs leverage the image semantics for mapping, it is necessary to clarify the semantic granularity. Existing research on adversarial perturbations [4, 31] and image classification [9, 16] focuses on the salient feature of the image (e.g., distinguishing between cats and dogs), which corresponds to coarse-grained semantics. In contrast, images can also be categorized according to fine-grained semantics (e.g., the specific dog apart from other dogs).

To bridge this gap and provide a more comprehensive assessment of the flexible threats posed by SAUPs, we propose *Real Image Sequence Trajectories (RIST)*, an image dataset annotated with fine-grained semantics. RIST comprises over 1,000 images and 28 trajectories, collected from real-world videos and encompassing two representative scenarios: autonomous driving and robot tasking. As shown in Figure 3, RIST defines each class as a sequence of semantically coherent images, and each trajectory consists of multiple such classes extracted from a single video. Further details can be found in the Appendix.



Figure 3. Illustration of RIST, which consists of real-world image trajectories across two scenarios: AutoDriving and RoboTasking. RIST clusters semantically similar frames as the same class, with each class containing 10 images.

By utilizing fine-grained semantic granularity, SAUPs enable attackers to flexibly orchestrate events. For instance, in the context of vision-based robotics, an image containing a knife (target action: hold) and an image featuring both a knife and a human (target action: throw) can be considered distinct semantic classes.

3.2. Normalized Space Optimization

To facilitate the addition of perturbations to images, existing studies [4, 23, 34, 35] conduct their optimization directly in the pixel space ([0, 1]). While this approach is sufficient for existing attack objectives, it is inadequate for the stringent restrictions required by SAUP. Consequently, we are motivated to shift the optimization process to a more effective representation space, where the search for viable perturbations becomes more tractable.

We refer to the space after image normalization as an effective domain for searching SAUPs for the following reasons: 1) The loss landscape in the normalized space is smoother [19], resulting in stable gradients and fewer local optima. This benefits gradient-based optimization methods, making it easier to generate feasible perturbations. 2) Representations in the normalized space tend to have similar scales, enabling the optimizer to take consistent step sizes across the loss landscape. This leads to a more stable search along different dimensions.

We now formalize this optimization process. Let $f_{\mathcal{T}}: \mathcal{V} \to \mathcal{Z}$ denote the image normalization. Given a clean image $\mathbf{x} \in \mathcal{V}$, where pixel values are bounded within [0,1], and a perturbation constraint mask \mathbf{r} , we can first map these values into space \mathcal{Z} for subsequent search:

$$\mathbf{Z} = f_{\mathcal{T}}(\mathbf{x}), \quad \Delta = f_{\mathcal{T}}(\delta), \quad \mathbf{R} = f_{\mathcal{T}}(\mathbf{r})$$

$$\mathbf{Z} = f_{\mathcal{T}}(\mathbf{0}), \quad \mathbf{\overline{Z}} = f_{\mathcal{T}}(\mathbf{1})$$
(3)

Then, we can focus on the model inference stage $f_{\mathcal{M}}$ and reformulate the optimization objective in Eq.(1) as follows:

$$\arg\min_{\Lambda} \mathbb{E}_{\mathcal{D}} \left\{ \mathcal{L} \left(f_{\mathcal{M}} \left(\mathcal{A} \left(\mathbf{Z}^{(c)}, \mathbf{R} \right), \mathbf{p} \right), \mathbf{t}^{(c)} \right) \right\}$$
(4)

with a new constraint function:

$$\mathcal{A}(\mathbf{Z}, \Delta) = \left[\mathbf{Z} \cdot (\mathbf{1} - \mathbf{R}) + \Delta \cdot \mathbf{R}\right]_{\underline{\mathbf{Z}}}^{\overline{\mathbf{Z}}}$$
 (5)

According to Eq. (4), we can directly search for feasible solutions Δ within the normalized space. For each semantic clustering c, this objective binds the normalized inputs $\mathbf{Z}^{(c)}$ with their corresponding targets $\mathbf{t}^{(c)}$.

After completing the optimization, we obtain the optimal perturbation in the post-normalized space Δ^* . We can manually construct an approximately inverse transformation $f_{\mathcal{T}}^{-1}:\mathcal{Z}\to\mathcal{V}$, with a slight abuse of notation, to recover the adversarial perturbation δ in the pixel space.

$$\delta^* = f_{\mathcal{T}}^{-1}(\Delta^*) \tag{6}$$

Since the perturbation constraints are integrated into the optimization process, the resulting δ^* inherently satisfies the attacker's requirements.

3.3. Semantic Separation Optimization

Recall that the objective of SAUPs is to mislead MLLMs into generating a predefined target $\mathbf{t}^{(c)}$ corresponding to the class c of a given image. This target $\mathbf{t}^{(c)}$ typically consists of multiple tokens, which can also be denoted as $t_{1:N}^{(c)}$. Empirically, we observe that the model often assigns

Empirically, we observe that the model often assigns high confidence to all targets, and in some cases, the model generates target content that is misaligned with the input image (i.e., $\mathbf{t}^{(\neg c)}$). This situation is exacerbated for MLLMs, and the model may generate unintended content by combining tokens across various targets (e.g., $t_{>i}^{(c)} \oplus t_{>i}^{(\neg c)}$).

This motivates us to design a proper loss function that not only enhances the alignment between inputs and corresponding targets, but also separates the target labels from each other. To this end, we devise the semantic separation optimization, leveraging cross-entropy loss and margin-based loss. The overall loss function is formulated as follows:

$$\mathcal{L} = \mathcal{L}_{CE} + \lambda \cdot \mathcal{L}_{Margin} \tag{7}$$

where \mathcal{L}_{CE} and \mathcal{L}_{Margin} denote the cross-entropy loss and the margin loss, respectively. The λ is a weighting factor that balances the contributions of the two losses.

Cross-Entropy Guidance for Targets Generation. The cross-entropy loss is a standard approach for inducing specific outputs from MLLMs, inherently enhancing the alignment between inputs and targets within the same semantic cluster. It is defined as follows:

$$\mathcal{L}_{CE} = -\sum_{i=1}^{N} \log P_{\mathcal{M}} \left(t_i^{(c)} \mid t_{< i}^{(c)}, \mathcal{A} \left(\mathbf{Z}^{(c)}, \Delta \right), \mathbf{p} \right)$$
(8)

where $P_{\mathcal{M}}$ refers to the probability of the token sequence conditioned on the representation of the normalized space. Inter-Class Discrimination via Margin Loss. To encourage semantic-aware behavior and prevent target obfuscation, we introduce a margin loss that explicitly enforces separation between different targets.

Given an image with the semantic class c and its corresponding target $\mathbf{t}^{(c)}$, we compute the margin loss by measuring the difference in confidence between its correct target $\mathbf{t}^{(c)}$ and all other targets $\mathbf{t}^{(\neg c)}$. These differences are then clipped at zero, and their average is taken as the loss value.

For brevity, we denote $P_{\mathcal{M}}(\mathbf{t})$ as a shorthand for the conditional probability $P_{\mathcal{M}}(\mathbf{t} \mid \mathcal{A}(\mathbf{Z}, \Delta), \mathbf{p})$. Accordingly, the margin loss can be formally given by:

$$\mathcal{L}_{\text{Margin}} = \mathbb{E}_{i \neq c} \left\{ \left| m - P_{\mathcal{M}} \left(\mathbf{t}^{(c)} \right) + P_{\mathcal{M}} \left(\mathbf{t}^{(i)} \right) \right|_{0} \right\} \tag{9}$$

where m > 0 is a predefined margin enforcing a minimum separation, and $|\cdot|_0 = \max(0,\cdot)$.

4. Latent Space Analysis

In this section, we analyze the latent-space features of images perturbed by SAUPs and reveal three observations. Based on these observations, we propose an explanation for the semantic-aware ability of SAUPs, that is, why a perturbation can discern the semantics of images and assign different targets accordingly.

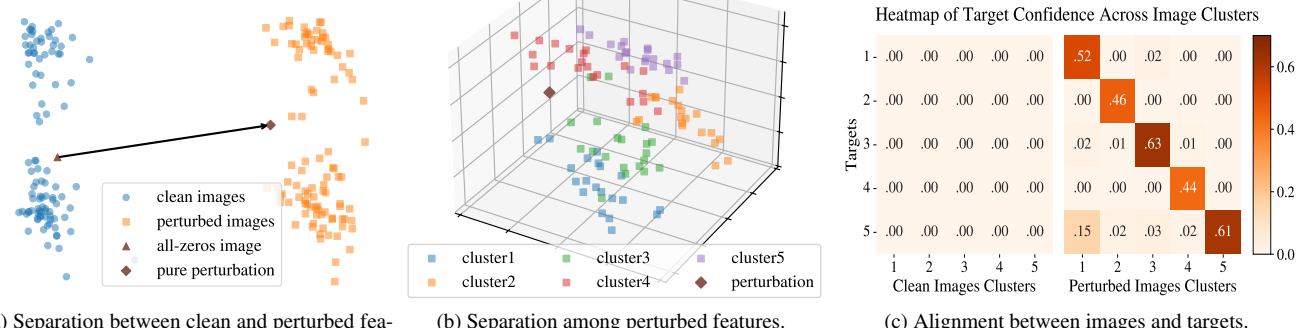
Empirical Observations in the Latent Space. We conduct experiments by searching for an SAUP on Llava-1.5-7B [22] using images from five distinct classes of ImageNet [9]. For each class, we randomly select 20 images and assign a unique word as the target label. We then extract and visualize the latent features from the model's penultimate layer.

As shown in Figure 4, our investigation of the latent space yields three progressive observations:

Separation of Clean and Perturbed Features. First, we observe a clear separation between the features of clean and perturbed images. To visualize this, we perform principal component analysis (PCA) on the extracted features. As shown in Figure 4a, the features of perturbed images are clustered together, far from the widely dispersed features of the original clean images. This indicates that the SAUP imposes a dominant influence on the features.

Semantic Separation within Perturbed Features. Second, while the perturbed features are grouped together, they are not monolithic. A closer look reveals that they form distinct sub-clusters based on their semantics. Figure 4b visualizes the perturbed features in a 3D view, showing that features corresponding to different semantics occupy separate spaces. This suggests the perturbed features are deflected by their original semantics.

Alignment of Semantic Clusters with Target Labels. Finally, we observe that these semantically segregated clusters are precisely aligned with their designated targets. We compute the average output confidence for each target, as illustrated in Figure 4c. The high values along the diagonal confirm that perturbed images from a specific semantic class consistently elicit a high confidence score for their



(a) Separation between clean and perturbed fea-

(b) Separation among perturbed features.

(c) Alignment between images and targets.

Figure 4. We generate a SAUP for Llava and extract image features from the penultimate layer. (a) The perturbation dominates the features of the perturbed images and deviates significantly from those of the clean images. (b) The perturbed image features corresponding to different semantics are separated from each other and occupy distinct locations in the feature space. (c) The perturbed images are aligned with their corresponding targets, resulting in high output confidence for those targets.

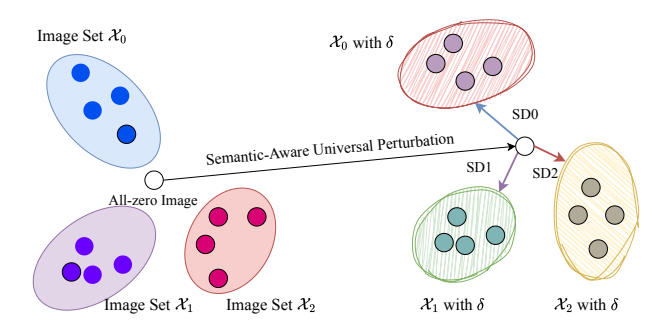


Illustration of the underlying mechanism of the Semantic-Aware phenomenon. Given three image sets V_0, V_1, V_2 with distinct semantic contents, and an all-zero pixel image serving as an anchor. The SAUP maps all image features to a distant region in the latent space, while the respective semantic directions (SDs) of \mathcal{V}_0 , \mathcal{V}_1 , \mathcal{V}_2 cause slight deflections in these features, guiding them towards alignment with predefined targets.

predefined target. This demonstrates that, after semantic deflection, the perturbed features are well aligned with their predefined targets in the latent space.

Explanation for the Semantic-Aware Phenomenon. Based on these observations, we propose an explanation for the semantic-aware nature of SAUPs. We posit that: Image features under the SAUP are dominated by the perturbation and slightly deflected according to the image semantics.

This mechanism can be understood with a simple model, as illustrated in Figure 5. Let's consider image sets $\mathcal{X}_0, \mathcal{X}_1, \mathcal{X}_2$ with distinct semantics. The SAUP introduces a common directional vector to all images, pulling their features into a specific region of the latent space, far from their "clean" locations. We can conceptualize this "pure" perturbation feature by applying the SAUP to an anchor image with no semantic content (e.g., an all-zero image).

Meanwhile, the inherent semantic content provides a

smaller, secondary vector that deflects the feature away from this pure perturbation point. Since different classes (e.g., \mathcal{X}_0 vs. \mathcal{X}_1) have different semantic directions, the perturbed features are deflected into separate spatial clusters.

Therefore, the optimization algorithm can be viewed as searching for a point in the latent space such that the spatial clusters formed by the deflected features are aligned with the predefined targets. By aligning different perturbed feature clusters with their corresponding targets, the perturbation appears to acquire the ability to "actively" recognize the semantics of images and assign targets accordingly.

5. Experiments

5.1. Experimental Setup

Datasets. We evaluate the effectiveness and generalization of SAUPs on two datasets.

- (1) ImageNet. To assess the effectiveness of SAUPs on coarse-grained semantics, we employ the ImageNet [9], which serves as a widely used benchmark in prior adversarial studies [7, 10]. We first randomly select C classes from ImageNet. For each class, 50 images are used as the training set (i.e., $50 \times C$ images in total), and another 20 non-overlapping images are used as the test set. The target for each class is randomly selected from the remaining categories and is represented by a single word; sentence-level targets are evaluated in Section 5.3.
- (2) RIST. To assess the effectiveness of SAUPs on finegrained semantics, we annotate and evaluate the RIST dataset. RIST consists of similar frames extracted from real-world videos, covering two scenarios: AutoDriving and RoboTasking with 5 and 2 classes, respectively. Each class contains 10 images, as well as a manually annotated word serving as the target. The 5 images are used for training, and the remaining 5 images are used for testing.

For collecting RIST, our annotators meticulously iden-



Figure 6. Attack success rates versus the number of targets (#targets) on the ImageNet. The frame refers to adding a narrow border around an image, while the corner refers to attaching patches to the four corners of an image.

tify segments that contain potential risks and exclude repetitive or semantically meaningless segments. Each category within the RIST dataset contains sequences centered around a specific event, such as robots interacting with kitchen utensils or cars passing through intersections with pedestrians and warning signs.

To ensure each sequence captures a unique event while maintaining diversity between different sequences, our annotators review more than 1 TB of video frames and manually filter out highly similar images. We ensure that every image in the RIST dataset is independently cross-validated by two annotators to guarantee quality and consistency. More details can be found in the Appendix.

Models. Our experiments involve three representative MLLMs. (1) *LLaVA-1.5-7B* (*Llava*) [22] is a widely used open-source MLLM that has been extensively used as a benchmark in prior studies [17, 23]. (2) *Qwen2.5-VL-7B-Instruct* (*Qwen*) [3] is a well-known model that incorporates advanced instruction-following abilities. (3) *InternVL3-8B* (*Intern*) [42] is designed for strong general-purpose vision and language understanding, with competitive performance across multiple vision-language tasks [11].

Following [23], we default to fixing the user input prompt $\bf p$ as Describe this image, and utilize greedy decoding for both MLLMs. We also evaluate attack performance under varying input prompts in the Appendix. **Perturbation Constraints.** Consistent with prior work [23], we focus on two types of constrained adversarial perturbations: *frame* and *corner*, where the frame width is set to 6 pixels, and each corner patch has a size of 20×20 pixels unless otherwise specified 2 . We also involve more constraint settings in the Appendix.

Evaluation Metric. Following [23, 31], we report the *Attack Success Rate (ASR)* as the evaluation metric. ASR is a simple yet stringent measure, as it requires the model's pre-

dictions to exactly match the predefined target sequences.

Given a dataset $\mathcal{D} = \{(\mathbf{x}'_i, \mathbf{t}_i)\}_{i=1}^{|\mathcal{D}|}$, where each \mathbf{x}'_i is a perturbed image and \mathbf{t}_i is its corresponding target (a word or a sentence), the ASR is formally defined as:

$$ASR = \frac{1}{|\mathcal{D}|} \sum_{i=1}^{|\mathcal{D}|} \mathbb{I}[f(\mathbf{x}_i', \mathbf{p}) = \mathbf{t_i}]$$
 (10)

where $\mathbb{I}[\cdot]$ is the indicator function that returns 1 if the condition is true, and 0 otherwise.

Considering the model may require outputting many tokens to convey meaningful content, these tokens must match the target sequence in both content and order. This strict metric captures the ability of SAUPs to exert precise control, which is essential for downstream applications.

Implementation Details. The experiments are conducted using seven NVIDIA RTX 3090 GPUs. Consistent with previous work [23], each SAUP is generated over 500 epochs. We employ the Momentum optimizer [10] with a momentum of 0.9, a learning rate of 0.01, and set the margin loss weighting factor to 1. During inference, greedy decoding is adopted, that is, the token with the highest confidence is selected at each step.

5.2. Vulnerability Analysis of MLLMs

5.2.1. Results on the ImageNet

We assess the effectiveness of SAUPs with different numbers of targets (#targets) on ImageNet. As shown in Figure 6, we have the following findings:

(1) MLLMs exhibit significant vulnerability to SAUPs. When misleading five targets, we achieve the ASR over 63% and 45% with frame and corner constraints, respectively. Notably, when attacking 9 targets under the frame constraint, we still achieve ASRs of 42% on Llava, 31% on Qwen, and 48% on Intern. These results demonstrate that SAUPs can effectively aware the semantics of input images and steer the model toward distinct targets.

 $^{^2}$ These perturbation constraints are defined for an image of size 300×300 [5, 31]. For fair comparison across models, we linearly scale constraints according to the specific input size required by each model.

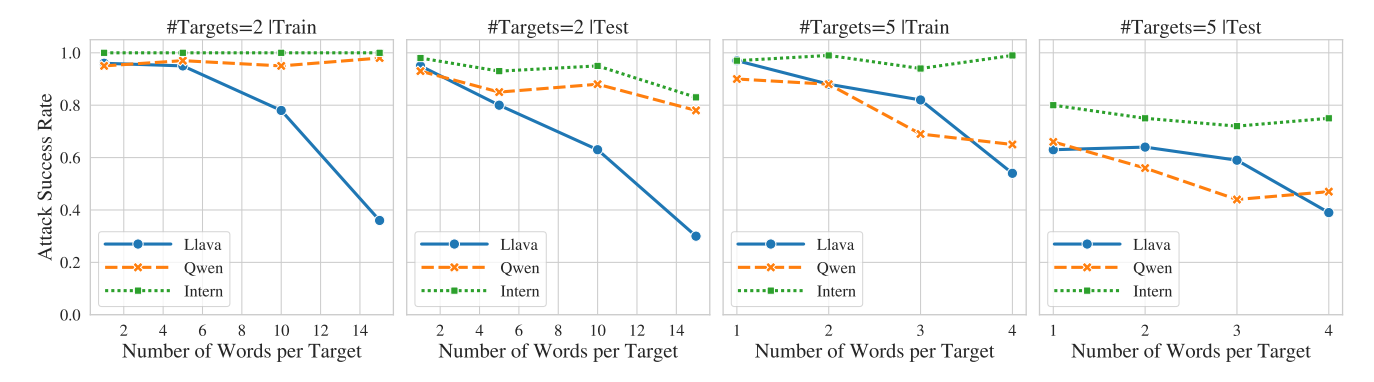


Figure 7. Attack success rates under different numbers of targets (#Targets) and words per target.

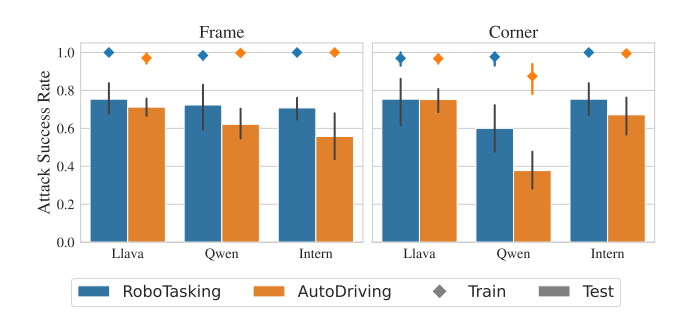


Figure 8. Attack success rates of SAUP on each trajectory of the RIST dataset, covering two realistic scenarios, RoboTasking (#Targets=2) and AutoDriving (#Targets=5).

- (2) The ASR exhibits a decreasing trend as #targets increases. We evaluated SAUP's performance with one to nine targets and observed a general decline in ASR as the number of targets grew. Among the different model types, Intern demonstrated the greatest susceptibility, as its ASR curve decreased more gradually than the others.
- (3) The perturbation constraint plays a critical role in determining ASR. For Llava and Qwen, the ASR of corner-based perturbations drops to 0 when the number of targets reaches eight. This phenomenon can be attributed to the disparity in the number of modifiable pixels, 1,600 for corners versus 7,056 for the frame. In contrast, corner-based perturbations achieve comparable ASR with a small number of targets because their perturbations are spatially concentrated, allowing them to effectively manipulate features.

5.2.2. Results on the RIST

In this subsection, we evaluate the performance of SAUPs on the RIST dataset. Unlike traditional classification datasets, RIST focuses on fine-grained semantic understanding and covers two scenarios: RoboTasking (2 categories) and AutoDriving (5 categories). We summarize the ASR for each trajectory, as shown in Figure 8.

The results demonstrate that we can generate effective

SAUPs based on fine-grained semantic image clustering. On the test sets of the RoboTasking and AutoDriving scenarios, we achieve an average ASR of 72% and 62%, respectively. These results highlight the flexibility and efficiency of SAUP generation, revealing that attackers can craft highly effective perturbations from only five images, thereby posing a significant security risk.

The overfitting phenomenon occurs during the SAUP generation. For example, we achieve a 100% ASR on the training set for Intern for both scenarios, yet the average ASR drops to 73% and 61% on the test set, respectively. This overfitting arises from the limited training set of RIST, which involves at most 50 images for training, making it easy for the SAUP to overfit. We think this issue can be mitigated by increasing the size of the training set and incorporating multiple image augmentation strategies.

5.3. Evaluation of Sentence Control

Precise control over sentence-level outputs expands the application of image hijacks, enabling scenarios such as spreading misinformation and executing malicious commands. This subsection evaluates the SAUPs' ability to control sentence-level output by varying the number of words per target (#words per target). In other words, the SAUP is expected to compel the MLLM to generate sentences that exactly match the predefined targets for different images.

We evaluate the attack performance under the frame constraint by using up to 15 words for 2 targets and up to 4 words for 5 targets. As illustrated in Figure 7, we can have the following observations:

SAUPs are effective in controlling MLLMs to generate sentences. Impressively, when each target consists of 10 words under 2 targets, we still achieve an average ASR of 83% on the test set. When the number of targets increases to 5, SAUPs are still able to control 4 words per target, achieving 54% average ASR on the test set.

The Qwen and Intern are highly susceptible to control by SAUPs, enabling the precise generation of sentences. For example, when reaching 15 words under 2 targets, we

Table 1. Ablation studies on the c	optimization algorithm components.	with bold indicating the highest ASR on the test set.

	Constraint	aint Frame										Corner							
Model	Method	Base	line	w/o NSO			w/o MarginLoss		Default		Baseline		w/o NSO		o nLoss	Default			
	#Targets	Train	Test	Train	Test	Train	Test	Train	Test	Train	Test	Train	Test	Train	Test	Train	Test		
Llava	2	0.00	0.00	0.03	0.00	0.93	0.93	0.96	0.95	0.05	0.03	0.23	0.13	1.00	0.93	0.90	0.88		
Liava	5	0.13	0.11	0.46	0.43	0.82	0.57	0.97	0.63	0.48	0.47	0.01	0.03	0.51	0.40	0.67	0.49		
Qwen	2	0.00	0.00	0.00	0.00	0.99	0.93	0.95	0.93	0.35	0.33	0.40	0.38	0.98	0.95	1.00	0.98		
Qwen	5	0.01	0.03	0.02	0.00	0.72	0.57	0.90	0.66	0.15	0.15	0.12	0.19	0.46	0.44	0.63	0.45		
Intern	2	0.98	0.83	0.95	0.78	1.00	0.97	1.00	0.98	0.95	0.80	0.78	0.55	1.00	0.98	1.00	1.00		
mem	5	0.84	0.76	0.78	0.73	0.82	0.76	0.97	0.80	0.86	0.84	0.50	0.40	0.95	0.79	0.92	0.82		

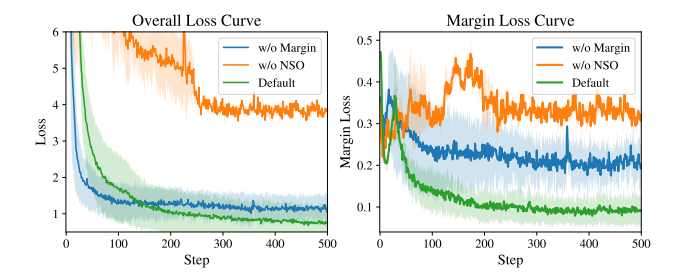


Figure 9. Loss curve during SAUPs optimization for the Qwen with 5 targets. The absence of NSO causes the loss to remain consistently high and prevents effective reduction during optimization. Removing the margin loss leads the optimization process to converge to local optima.

achieve 78% ASR on Qwen and 83% ASR on Intern. This suggests that these models are heavily impacted by incorrect tokens in the preceding generation, which in turn makes the subsequent sequence more prone to being erroneous.

5.4. Ablation Studies

This subsection presents ablation studies to analyze the individual contributions of the two components in the proposed method, i.e., the normalized space optimization and the semantic separation optimization.

We first introduce two variants of the SORT: (1) w/o NSO, which removes the normalized space optimization module and directly optimizes SAUPs in the [0,1] pixel space; (2) w/o MarginLoss, which eliminates the margin loss function and relies solely on the cross-entropy loss for optimization. We also adapt the existing image hijack [4] for multiple targeted scenarios to serve as a baseline.

We conduct experiments with #targets set to 2 and 5 on these variants. As shown in Table 1, the default method achieves the highest ASR across most settings, indicating the effectiveness of both components. We also visualize the global loss and margin loss on Qwen with 5 targets in Figure 9. In the following, we provide an in-depth analysis of

two components, respectively.

The NSO module provides the foundation for optimization, ensuring the effectiveness of the SORT. Specifically, Table 1 shows that the absence of NSO leads to an average 49.5% decrease in ASR on the test set. Figure 9 further indicates that, without NSO, the loss becomes trapped in a plateau, making it difficult for the optimization to converge to an optimal solution. These results suggest that NSO is a fundamental component in the optimization of SAUPs.

The semantic separation module improves the effectiveness of the SORT, particularly as #targets increases. As shown in Table 1, the w/o MarginLoss variant achieves a comparable ASR to the default setting when #targets is two, as the optimization difficulty remains low and cross-entropy loss alone is sufficient to guide the attack. However, as #targets increases, the margin loss yields an average ASR gain of 6%. Figure 9 also shows that although the variant without margin loss converges faster initially, it ultimately tends to get trapped in a local optimum.

6. Conclusion

This paper demonstrates the feasibility of hijacking the decision chain of neural networks through a single perturbation, which compels the model to precisely output different predefined targets based on the input semantics. To address the optimization challenges posed by the alignment of input semantics and predefined targets, we introduce SORT, an effective algorithm that incorporates a normalized space optimization and a semantic separation strategy. We further introduce RIST, a newly annotated dataset to evaluate the attack performance under fine-grained semantic granularity.

We perform an in-depth analysis of perturbed and clean image features in the latent space to explain the underlying reasons for the semantic-aware ability. We conduct extensive experiments on both ImageNet and RIST datasets on three representative MLLMs and two perturbation constraints. The results demonstrate the effectiveness and generalization capability of SAUPs. For future work, we intend

to develop robust and transferable SAUPs that can be deployed in the physical world. We hope this paper can inspire the discovery of novel security threats in neural networks.

References

- [1] Josh Achiam, Steven Adler, Sandhini Agarwal, Lama Ahmad, Ilge Akkaya, Florencia Leoni Aleman, Diogo Almeida, Janko Altenschmidt, Sam Altman, Shyamal Anadkat, et al. Gpt-4 technical report. arXiv preprint arXiv:2303.08774, 2023. 1
- [2] Jinze Bai, Shuai Bai, Shusheng Yang, Shijie Wang, Sinan Tan, Peng Wang, Junyang Lin, Chang Zhou, and Jingren Zhou. Qwen-vl: A frontier large vision-language model with versatile abilities. *arXiv preprint arXiv:2308.12966*, 1(2):3, 2023. 1, 2
- [3] Shuai Bai, Keqin Chen, Xuejing Liu, Jialin Wang, Wenbin Ge, Sibo Song, Kai Dang, Peng Wang, Shijie Wang, Jun Tang, et al. Qwen2. 5-vl technical report. arXiv preprint arXiv:2502.13923, 2025. 6
- [4] Luke Bailey, Euan Ong, Stuart Russell, and Scott Emmons. Image hijacks: Adversarial images can control generative models at runtime. *arXiv preprint arXiv:2309.00236*, 2023. 1, 2, 3, 8, 14
- [5] Wieland Brendel, Jonas Rauber, and Matthias Bethge. Decision-based adversarial attacks: Reliable attacks against black-box machine learning models. *arXiv preprint arXiv:1712.04248*, 2017. 6
- [6] Nicholas Carlini and David Wagner. Towards evaluating the robustness of neural networks. In 2017 ieee symposium on security and privacy (sp), pages 39–57. Ieee, 2017. 2
- [7] Jianbo Chen, Michael I Jordan, and Martin J Wainwright. Hopskipjumpattack: A query-efficient decision-based attack. In 2020 ieee symposium on security and privacy (sp), pages 1277–1294. IEEE, 2020. 5
- [8] Google DeepMind. The gemini family. https: //deepmind.google/technologies/gemini/, 2025. Multimodal large language model family. 1, 11
- [9] J. Deng, W. Dong, R. Socher, L.-J. Li, K. Li, and L. Fei-Fei. ImageNet: A Large-Scale Hierarchical Image Database. In CVPR09, 2009. 2, 3, 4, 5
- [10] Yinpeng Dong, Fangzhou Liao, Tianyu Pang, Hang Su, Jun Zhu, Xiaolin Hu, and Jianguo Li. Boosting adversarial attacks with momentum. In 2018 IEEE Conference on Computer Vision and Pattern Recognition, CVPR 2018, Salt Lake City, UT, USA, June 18-22, 2018, pages 9185–9193. Computer Vision Foundation / IEEE Computer Society, 2018. 5,
- [11] Haodong Duan, Junming Yang, Yuxuan Qiao, Xinyu Fang, Lin Chen, Yuan Liu, Xiaoyi Dong, Yuhang Zang, Pan Zhang, Jiaqi Wang, et al. Vlmevalkit: An open-source toolkit for evaluating large multi-modality models. In *Proceedings* of the 32nd ACM International Conference on Multimedia, pages 11198–11201, 2024. 6
- [12] Hao Fang, Jiawei Kong, Wenbo Yu, Bin Chen, Jiawei Li, Hao Wu, Shutao Xia, and Ke Xu. One perturbation is enough: On generating universal adversarial perturbations

- against vision-language pre-training models. arXiv preprint arXiv:2406.05491, 2024. 1, 2
- [13] Stanislav Fort. Multi-attacks: Many images+ the same adversarial attack→ many target labels, 2023. URL https://arxiv. org/abs/2308.03792, 2023. 2
- [14] Ian J Goodfellow, Jonathon Shlens, and Christian Szegedy. Explaining and harnessing adversarial examples. *arXiv* preprint arXiv:1412.6572, 2014. 2
- [15] Xiaojun Jia, Sensen Gao, Simeng Qin, Tianyu Pang, Chao Du, Yihao Huang, Xinfeng Li, Yiming Li, Bo Li, and Yang Liu. Adversarial attacks against closed-source mllms via feature optimal alignment. arXiv preprint arXiv:2505.21494, 2025.
- [16] Ziheng Jia, Zicheng Zhang, Jiaying Qian, Haoning Wu, Wei Sun, Chunyi Li, Xiaohong Liu, Weisi Lin, Guangtao Zhai, and Xiongkuo Min. Vqa²: Visual question answering for video quality assessment, 2024. 3
- [17] Hee-Seon Kim, Minbeom Kim, and Changick Kim. Doubly-universal adversarial perturbations: Deceiving vision-language models across both images and text with a single perturbation. *arXiv* preprint arXiv:2412.08108, 2024. 6
- [18] Moo Jin Kim, Karl Pertsch, Siddharth Karamcheti, Ted Xiao, Ashwin Balakrishna, Suraj Nair, Rafael Rafailov, Ethan Foster, Grace Lam, Pannag Sanketi, et al. Openvla: An open-source vision-language-action model. arXiv preprint arXiv:2406.09246, 2024. 1, 2
- [19] Hao Li, Zheng Xu, Gavin Taylor, Christoph Studer, and Tom Goldstein. Visualizing the loss landscape of neural nets. Advances in neural information processing systems, 31, 2018.
- [20] Jiadong Lin, Chuanbiao Song, Kun He, Liwei Wang, and John E Hopcroft. Nesterov accelerated gradient and scale invariance for adversarial attacks. arXiv preprint arXiv:1908.06281, 2019. 14
- [21] Daizong Liu, Mingyu Yang, Xiaoye Qu, Pan Zhou, Xiang Fang, Keke Tang, Yao Wan, and Lichao Sun. Pandora's box: Towards building universal attackers against real-world large vision-language models. In *The Thirty-eighth Annual Con*ference on Neural Information Processing Systems, 2024. 2
- [22] Haotian Liu, Chunyuan Li, Qingyang Wu, and Yong Jae Lee. Visual instruction tuning. *Advances in neural information processing systems*, 36:34892–34916, 2023. 1, 2, 4, 6
- [23] Dong Lu, Tianyu Pang, Chao Du, Qian Liu, Xianjun Yang, and Min Lin. Test-time backdoor attacks on multimodal large language models. *arXiv preprint arXiv:2402.08577*, 2024. 1, 2, 3, 6, 14
- [24] Haochen Luo, Jindong Gu, Fengyuan Liu, and Philip Torr. An image is worth 1000 lies: Transferability of adversarial images across prompts on vision-language models. In *The Twelfth International Conference on Learning Representa*tions, 2024. 1, 2, 14
- [25] Jiageng Mao, Minzhe Niu, Chenhan Jiang, Hanxue Liang, Jingheng Chen, Xiaodan Liang, Yamin Li, Chaoqiang Ye, Wei Zhang, Zhenguo Li, et al. One million scenes for autonomous driving: Once dataset. arXiv preprint arXiv:2106.11037, 2021. 2, 11

- [26] Seyed-Mohsen Moosavi-Dezfooli, Alhussein Fawzi, Omar Fawzi, and Pascal Frossard. Universal adversarial perturbations. In *Proceedings of the IEEE conference on computer* vision and pattern recognition, pages 1765–1773, 2017. 1, 2, 14
- [27] Muzammal Naseer, Salman Khan, Munawar Hayat, Fahad Shahbaz Khan, and Fatih Porikli. On generating transferable targeted perturbations. In *Proceedings of the IEEE/CVF International Conference on Computer Vision (ICCV)*, pages 7708–7717, 2021. 1, 2, 14
- [28] Xiangyu Qi, Kaixuan Huang, Ashwinee Panda, Peter Henderson, Mengdi Wang, and Prateek Mittal. Visual adversarial examples jailbreak aligned large language models. In *Proceedings of the AAAI conference on artificial intelligence*, pages 21527–21536, 2024. 1, 2
- [29] Rylan Schaeffer, Dan Valentine, Luke Bailey, James Chua, Cristobal Eyzaguirre, Zane Durante, Joe Benton, Brando Miranda, Henry Sleight, Tony Tong Wang, et al. Failures to find transferable image jailbreaks between vision-language models. In *The Thirteenth International Conference on Learning Representations*, 2024. 14
- [30] Erfan Shayegani, Yue Dong, and Nael Abu-Ghazaleh. Jailbreak in pieces: Compositional adversarial attacks on multimodal language models. In *The Twelfth International Con*ference on Learning Representations, 2024. 2
- [31] Meng Shen, Changyue Li, Qi Li, Hao Lu, Liehuang Zhu, and Ke Xu. Transferability of white-box perturbations: query-efficient adversarial attacks against commercial dnn services. In 33rd USENIX Security Symposium (USENIX Security 24), pages 2991–3008. USENIX Association, 2024. 3, 6
- [32] Christian Szegedy, Wojciech Zaremba, Ilya Sutskever, Joan Bruna, Dumitru Erhan, Ian Goodfellow, and Rob Fergus. Intriguing properties of neural networks, 2014. 2
- [33] Chen Tang, Ben Abbatematteo, Jiaheng Hu, Rohan Chandra, Roberto Martín-Martín, and Peter Stone. Deep reinforcement learning for robotics: A survey of real-world successes. In *Proceedings of the AAAI Conference on Artificial Intelli*gence, pages 28694–28698, 2025. 11
- [34] Viet Quoc Vo, Ehsan Abbasnejad, and Damith C. Ranasinghe. Ramboattack: A robust and query efficient deep neural network decision exploit. In 29th Annual Network and Distributed System Security Symposium, NDSS 2022, San Diego, California, USA, April 24-28, 2022. The Internet Society, 2022. 3
- [35] Xiaosen Wang and Kun He. Enhancing the transferability of adversarial attacks through variance tuning. In *Proceedings* of the IEEE/CVF conference on computer vision and pattern recognition, pages 1924–1933, 2021. 3, 14
- [36] Zhibo Wang, Hongshan Yang, Yunhe Feng, Peng Sun, Hengchang Guo, Zhifei Zhang, and Kui Ren. Towards transferable targeted adversarial examples. In *Proceedings of the IEEE/CVF conference on computer vision and pattern recognition*, pages 20534–20543, 2023. 2
- [37] Binyan Xu, Xilin Dai, Di Tang, and Kehuan Zhang. One surrogate to fool them all: Universal, transferable, and targeted adversarial attacks with clip, 2025. 2
- [38] Jiazhi Yang, Shenyuan Gao, Yihang Qiu, Li Chen, Tianyu Li, Bo Dai, Kashyap Chitta, Penghao Wu, Jia Zeng, Ping Luo,

- et al. Generalized predictive model for autonomous driving. In *Proceedings of the IEEE/CVF Conference on Computer Vision and Pattern Recognition*, pages 14662–14672, 2024. 1, 2, 11
- [39] Zonghao Ying, Aishan Liu, Tianyuan Zhang, Zhengmin Yu, Siyuan Liang, Xianglong Liu, and Dacheng Tao. Jailbreak vision language models via bi-modal adversarial prompt. arXiv preprint arXiv:2406.04031, 2024. 2
- [40] Jiaming Zhang, Junhong Ye, Xingjun Ma, Yige Li, Yunfan Yang, Jitao Sang, and Dit-Yan Yeung. Anyattack: Towards large-scale self-supervised generation of targeted adversarial examples for vision-language models. *arXiv preprint arXiv:2410.05346*, 2024. 2
- [41] Yunqing Zhao, Tianyu Pang, Chao Du, Xiao Yang, Chongxuan Li, Ngai-Man Man Cheung, and Min Lin. On evaluating adversarial robustness of large vision-language models. *Advances in Neural Information Processing Systems*, 36:54111–54138, 2023. 2
- [42] Jinguo Zhu, Weiyun Wang, Zhe Chen, Zhaoyang Liu, Shenglong Ye, Lixin Gu, Hao Tian, Yuchen Duan, Weijie Su, Jie Shao, et al. Internvl3: Exploring advanced training and test-time recipes for open-source multimodal models. *arXiv* preprint arXiv:2504.10479, 2025. 6

A. Design Details of RIST Dataset

We introduce the Real Image Sequence Trajectories (RIST), a newly annotated dataset to evaluate adversary capacity to induce distinct, predefined targets by exploiting the fine-grained semantics. The fine-grained semantics are defined by a sequence of images with similar content, such as images of a specific intersection. This grants the adversary "switch-case" capability to "program" the incidents flexibly. For instance, a single perturbation could first guide an MLLM to output "grasp" when a robot observes a knife, and then trigger a dangerous action like "throw" when a human subsequently enters the scene.

A.1. Dataset Curation and Content

RIST consists of over 1,000 real-world images and 28 distinct trajectories, spanning two specialized sub-datasets: AutoDriving and RoboTasking. Each trajectory comprises multiple image sequences extracted from a continuous video with a consistent point of view (POV). We treat these image sequences as different categories based on finegrained semantics. Each image sequence consists of 10 visually similar frames and captures a specific action, such as driving through an intersection or picking up a cup.

To collect RIST, our annotators meticulously identify segments containing a specific event and exclude repetitive or semantically meaningless segments, such as cars idling at stoplights or robotic arms executing non-essential movements. Each category in the RIST dataset is centered around a specific event that could potentially be exploited for malicious purposes. For example, the image sequences include scenes of robots interacting with kitchen utensils or cars navigating intersections with warning signs.

To ensure that each sequence captures a unique event while preserving diversity across the dataset, our annotators review more than 1 TB of video footage and manually filter out highly similar images. Each image in RIST is independently cross-validated by two annotators to ensure both quality and diversity.

AutoDriving is designed to simulate the decision chain of a driving autonomous vehicle. It comprises 15 trajectories, each further segmented into 5 distinct categories. Each category is represented by a sequence of 10 POV images, formatted as 1920x1080 pixel JPG images. The initial POV driving videos for AutoDriving are sourced from the OpenDV-2K dataset [38] and the ONCE dataset [25]. This curation spans multiple countries and varies in temporal and meteorological conditions to ensure diversity.

RoboTasking is curated to evaluate the robustness of robotic decision chains in realistic indoor environments. It consists of 13 trajectories, each of which is divided into 2 categories. Similarly, each category comprises a sequence of 10 POV images, captured at a resolution of 320x180 pixels and stored as JPG files. The original POV robot videos

for RoboTasking are sourced from the DROID dataset [33], utilizing the robot's wrist-mounted camera perspective. We cover a wide range of robotic tasks (e.g., grasping objects, placing items, and operating tools) across various environments, including kitchens, living rooms, and workshops.

A.2. Target Action Annotation

To evaluate our semantic-aware universal perturbations (SAUPs), distinct targets are manually assigned for each category within the RIST, designed to guide the SAUP optimization towards inducing specific, contextually relevant yet undesirable behaviors from the MLLM. The annotation process for each sub-dataset is as follows:

For the AutoDriving, the image sequence corresponding to each category is input into Gemini-2.5-pro [8]. The model is prompted to act as an autonomous driving system and select a driving action based on the input images that would most likely pose a significant traffic safety risk. This selected action is assigned as the target for this category.

Similarly, for the RoboTasking, each image sequence is subsequently processed by the MLLM to produce the target. In this context, the model is instructed to play an embodied robot, and select a robotic action that would most likely introduce an operational safety hazard.

When evaluating RIST, all images are first scaled to a [0,1] pixel range. Within each category, half images are selected for the training set, used to optimize the SAUP. The remaining images serve as the test set to evaluate the SAUP's generalization.

B. Optimization Algorithm

This section presents a description of the optimization strategy for generating SAUPs, as illustrated in Algorithm 1.

Given an image dataset \mathcal{D} , the adversary assigns a target label to each image based on its category. Thus, we can reorganize \mathcal{D} such that each data entry consists of an image \mathbf{x} , a corresponding target label \mathbf{t} , and a query prompt \mathbf{p} .

For normalized space optimization, we first apply the image preprocessing function $f_{\mathcal{T}}$ to both the dataset \mathcal{D} and the initialized perturbation δ in lines 2. Each image \mathbf{x} in the dataset is transformed into a representation \mathbf{Z} , while the perturbation δ is transformed into Δ . To enable continuous optimization in the normalized space, we further transform the image bounds and perturbation constraints accordingly. In lines 3 of the algorithm, the image pixel value bounds, originally in the range [0,1], are transformed to the corresponding bounds $[\mathbf{Z},\overline{\mathbf{Z}}]$ in the normalized space. Simultaneously, the perturbation constraints are transformed into new region constraints \mathbf{R} .

For *semantic separation optimization*, we begin each optimization iteration by clipping the perturbed image with the new constraint, as shown in Line 6. These inputs are then

Table 2. Attack success rates of SAUPs	under various input prompts. Note that these	prompts are not in the training set.

			Qwen		Llava				Intern			
	Fr	ame	Corner		Frame		Corner		Frame		Corner	
Prompt	Train	Test	Train	Test	Train	Test	Train	Test	Train	Test	Train	Test
What is in the image?	0.97	0.85	0.98	0.93	0.02	0.03	0.00	0.00	0.81	0.65	1.00	1.00
What's happening in this picture?	0.76	0.63	0.91	0.90	0.18	0.13	0.26	0.25	0.97	0.80	1.00	0.98
Can you tell me about this image?	0.97	0.83	0.93	0.93	0.35	0.25	0.20	0.25	0.91	0.75	0.98	0.90
Summarize the content of this image.	0.97	0.80	0.96	0.93	0.38	0.35	0.20	0.13	0.90	0.83	0.98	0.93
Describe what you see in the photo.	0.93	0.83	0.97	0.98	0.31	0.25	0.19	0.15	0.55	0.40	0.99	0.95
Could you give me a general overview?	0.87	0.70	0.94	0.95	0.10	0.08	0.00	0.03	0.87	0.73	0.99	0.93
What colors dominate the image?	0.96	0.80	0.97	0.95	0.03	0.01	0.00	0.00	0.79	0.60	1.00	1.00
What is likely to happen next?	0.95	0.80	0.88	0.88	0.27	0.33	0.30	0.30	0.94	0.80	1.00	1.00
What message or story does this image convey?	0.75	0.55	0.86	0.85	0.18	0.25	0.01	0.03	0.97	0.95	1.00	0.98
What is the setting or location of this scene?	0.94	0.73	0.91	0.93	0.02	0.03	0.14	0.08	0.90	0.75	1.00	0.88

Algorithm 1: Optimization Algorithm for SAUPs

Input: Dataset \mathcal{D} , each entry consisting of an image \mathbf{x} , its corresponding target label \mathbf{t} , and user prompt \mathbf{p} . Semantic separation loss function \mathcal{L} . Image preprocess function $f_{\mathcal{T}}$. Perturbation constraint \mathbf{r} . Learning rate η .

Output: A semantic-aware universal perturbation δ .

```
1 Randomly initialize \delta;

2 \mathcal{D}', \Delta \leftarrow f_{\mathcal{T}}(D), f_{\mathcal{T}}(\delta);

3 \underline{\mathbf{Z}}, \overline{\mathbf{Z}}, \mathbf{R} \leftarrow f_{\mathcal{T}}(\mathbf{0}), f_{\mathcal{T}}(\mathbf{1}), f_{\mathcal{T}}(\mathbf{R});

4 for i \leftarrow 1 to Epoch do

5 | foreach \{\mathbf{Z}, \mathbf{t}, \mathbf{p}\} \in \mathcal{D}' do

6 | \mathbf{Z}' \leftarrow [\mathbf{Z} \cdot (1 - \mathbf{R}) + \mathbf{R} \cdot \Delta]_{\underline{\mathbf{Z}}}^{\overline{\mathbf{Z}}};

7 | L \leftarrow \mathcal{L}(\mathbf{Z}', \mathbf{t}; \mathbf{p});

8 | \Delta \leftarrow \Delta + \eta \cdot \nabla L;

9 | end

10 end

11 Construct inverse preprocess function f_{\mathcal{T}}^{-1};

12 \delta \leftarrow f_{\mathcal{T}}^{-1}(\Delta);

13 return \delta
```

fed into the dual-loss function \mathcal{L} , which integrates cross-entropy loss and margin loss. This objective not only enhances alignment between inputs and their assigned targets but also encourages separation among different target classes. Finally, the perturbation is updated via gradient descent using the learning rate η .

After completing the maximum number of optimization epochs, we manually construct an inverse transformation $f_{\mathcal{T}}^{-1}$ to map the optimized perturbation back to the original pixel space. The final perturbation δ can be generalized to unseen images, support multiple targets via semanticaware, and adhere to perturbation constraints.

C. Evaluation on Multiple Prompts.

To assess the robustness and generalization of SAUPs under diverse user queries, we evaluate the attack performance across a range of input prompts that vary in phrasing and semantic intent on ImageNet. Specifically, we utilize 50 different prompts in the training and 10 disjoint prompts in the evaluation. Table 2 summarizes the ASR of SAUPs on both training and testing sets under different prompt inputs.

We observe that SAUPs consistently achieve high ASRs on Qwen and Intern across prompts, with the average ASR of 74% and 94% under frame and corner constraints, respectively. Even when the prompts vary significantly, SAUPs remain effective in steering the model toward the predefined target outputs.

Contrary to intuition, Qwen and Intern, the more advanced MLLMs, demonstrate noticeably lower robustness than Llava when faced with diverse user prompts. Specifically, we achieve only a 14% ASR on Llava, which is substantially lower than the 84% obtained on Qwen and 84% on Intern. We think this is due to the deeper alignment between the visual encoder and the language model in advanced models. Specifically, Qwen and Intern employ full-parameter supervised fine-tuning to align visual and textual modalities, whereas Llava freezes the visual encoder and relies on a linear projection layer for alignment. This deeper alignment in advanced models may amplify the influence of adversarial perturbations on the subsequent language model, thereby reducing its overall robustness.

D. Impact of Perturbation Region

This section evaluates the SAUP on ImageNet by varying the perturbation frame width and the patch size of the corner. The results are shown in Table 3, which reveal that attack performance is highly dependent on the perturbation region.

TE 1 1 2 A	CATID 1 '		
Table 3. Attack success rates of	NALIPS linder various	nerfurbation region constrain	ntc .
Tuble 5. Tittuck success rates of	Di loi 5 unaci vanous	perturbation region constrain	LUG.

Llava									Qwen						Intern						
		Width of Frame Patch Size of Corner			Wid	Width of Frame Patch Size of Corner					Width of Frame Patch Size				Size of	ze of Corner					
	#Targets	4	6	8	20	30	40	4	6	8	20	30	40	4	6	8	20	30	40		
	2	0.90	0.97	1.00	0.90	1.00	1.00	0.92	0.95	1.00	1.00	0.96	0.99	0.98	1.00	1.00	1.00	1.00	1.00		
Train	4	0.56	0.97	0.94	0.94	0.96	1.00	0.42	0.93	0.92	0.63	0.87	0.92	0.95	1.00	1.00	0.95	1.00	1.00		
ıraın	6	0.30	0.92	0.96	0.75	0.92	0.94	0.35	0.85	0.85	0.56	0.63	0.86	0.67	0.96	0.98	0.94	0.98	0.99		
	8	0.44	0.75	0.81	0.00	0.41	0.64	0.20	0.55	0.64	0.00	0.47	0.69	0.54	0.96	0.86	0.66	0.73	0.84		
	2	0.53	0.85	0.93	0.88	1.00	1.00	0.63	0.93	1.00	0.98	0.90	0.98	0.90	0.98	1.00	1.00	1.00	1.00		
Test	4	0.31	0.64	0.93	0.69	0.90	0.94	0.30	0.61	0.84	0.43	0.79	0.86	0.64	0.81	0.94	0.80	0.91	0.99		
rest	6	0.11	0.58	0.72	0.61	0.84	0.82	0.23	0.53	0.60	0.37	0.57	0.86	0.38	0.64	0.91	0.93	0.85	0.88		
	8	0.22	0.41	0.56	0.00	0.37	0.51	0.16	0.26	0.43	0.00	0.33	0.58	0.29	0.61	0.59	0.49	0.54	0.69		

Table 4. Attack success rates under different sizes of training set

Model	Constraint			Size of Training Set									
Model	Constraint		10	20	30	40	50						
Llava	Frame	Train Test	1.00 0.10	1.00 0.53	0.93 0.58	0.93 0.83	0.96 0.95						
Liuvu	Corner	Train Test	1.00 0.45	1.00 0.75	0.98 0.88	0.94 0.83	0.90 0.88						
Owen	Frame	Train Test	1.00 0.85	0.98 0.63	0.92 0.85	0.96 0.95	0.95 0.93						
Qcii	Corner	Train Test	1.00 0.60	1.00 0.73	1.00 0.80	1.00 0.83	1.00 0.98						
Intern	Frame	Train Test	1.00 0.65	1.00 0.98	1.00 0.90	1.00 1.00	1.00 0.98						
	Corner	Train Test	1.00 0.65	1.00 0.90	1.00 0.85	1.00 1.00	1.00 1.00						

Expanding the frame width or enlarging the corner patch size substantially boosts the ASR. For instance, on the Llava test set with 8 targets, widening the adversarial frame from 4 to 8 pixels increases the ASR from 22% to 56%. Likewise, increasing the corner patch size from 20 to 40 yields a substantial improvement, raising ASR from 0% to 51%.

Enlarging the perturbation region can enhance the attack generalization. For example, when the number of targets is set to 4, increasing the frame width from 6 to 8 on the Llava yields similar ASR on the training set, but the ASR on the test set improves significantly from 64% to 93%. Likewise, for Qwen, increasing the corner patch size from 20 to 30 results in a 3% ASR gain on the training set, but leads to a substantial 30% improvement on the test set.

E. Impact of Training Set Size

This section evaluates the generalization of SAUPs by varying the size of the training set on ImageNet. Specifically, we generate SAUPs using subsets of 10, 20, 30, 40, and 50 im-

ages and evaluate their ASR on both the training and a fixed test set of 20 images. The results are summarized in Table 4.

We observe overfitting when the training set is small. For example, with 10 training samples, both Llava and Qwen achieve near-perfect ASR on the training set, but their performance drops significantly on the test set, especially for Llava under the frame constraint (10% ASR on test images). This discrepancy indicates that the learned perturbation may memorize training-specific features rather than generalize semantic alignment, limiting its real-world applicability.

On the contrary, increasing the training set size improves SAUPs' generalization to unseen data. For example, when the training set increases from 10 to 50 samples, Llava's test ASR under the frame constraint improves dramatically from 10% to 95%, showing that the learned perturbation begins to capture more generalizable features rather than overfitting to the training instances. Similarly, Qwen shows consistent improvements, especially under the corner constraint, where the test ASR reaches 98% with 50 training images. These trends highlight the importance of training diversity and sufficient semantic coverage for constructing transferable universal perturbations.

Meanwhile, a training set with only 50 images per class enables SAUPs to achieve strong attack performance even on unseen inputs. This suggests that an attacker could exploit a relatively limited but diverse set of images to capture the semantics of images and construct SAUPs effectively.

F. Analysis on Target Token Confidence

We analyze the confidence scores of perturbed images for five different targets. Since each target consists of one or more tokens, this section further decomposes each target into its tokens to display the confidence score of each token. As illustrated in Figure 10, we observe that perturbed images yield high confidence scores across multiple target tokens. For instance, Perturbed Image Cluster 1 displays elevated confidence for both token 2 and token 3 of Target 2. These results underscore the necessity of incorporating a

Table 5. Comparis	on of Adversaria	l Perturbation Me	thods.
-------------------	------------------	-------------------	--------

Category	Method Type	Mapping Relationship	Generalization	Semantic Binding	Threat & Complexity
Traditional Adversarial Perturbations	Untargeted	-	×	×	Low
Traditional Flavorsariai Fertaroations	Single Targeted	one-to-one	×	×	Low
Universal Adversarial Perturbations	Untargeted	-	✓	Х	Low
Chryersur Flaversur at 1 ertarourions	Single Targeted	many-to-one	✓	Х	Medium
SAUPs (This paper)	Multiple Targeted	many-to-many	1	✓	High

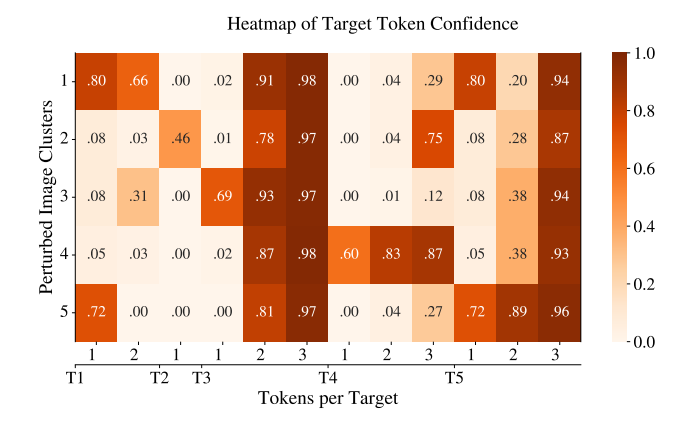


Figure 10. Illustration of confidence per tokens of each target, where Ti denotes the start of the i-th target.

semantic segmentation module in our design.

G. Discussion and Limitation

G.1. Discussion

This paper presents a novel threat model where the attacker can steer MLLMs to generate distinct targets based on the input semantics with a single perturbation. This grants the attacker a level of precision and control beyond traditional adversarial perturbations.

Current research on adversarial perturbations encounters limitations in flexibility, which can be categorized as shown in Table 5. Traditional adversarial perturbations [20, 35] are typically optimized on a per-instance basis. These methods can be either untargeted, aiming only to cause misclassification, or single-targeted, where the goal is to force the model to produce a specific incorrect label. However, these methods fail to scale or generalize to broader scenarios due to their inflexible, instance-specific design. Universal adversarial perturbations (UAPs) [26, 27] extend adversarial attacks by creating a single perturbation applicable across multiple inputs. Untargeted UAPs are effective in degrading model accuracy broadly, while single-targeted UAPs attempt to shift model predictions toward a fixed label across all inputs. Despite their improved generalization, the perturbations fail to provide fine-grained control over the output

based on the semantics of the input.

For seeking to manipulate multiple decisions towards distinct targets, existing approaches demand an individual perturbation for each input. This per-input generation makes them impractical for real-world applications, such as physically applying perturbations to every frame of a video.

In this context, SAUPs enable the adversary to freely map multiple images to various targets, representing a more sophisticated "switch-case" attack capability.

G.2. Limitation

While this paper demonstrates the existence and potential threat of SAUPs, it also has some limitations.

White-box Assumption and Transferability. This paper is based on the white-box assumption, where the attacker has full access to the target model's architecture and parameters. While this assumption is standard in current image hijack research [4], it poses a significant limitation in real-world scenarios, where models are often black boxes.

For cross-model transferability, prior work [29] has demonstrated that MLLMs are resistant to transfer attacks, and current studies on image hijacking [4, 23, 24] likewise have not observed cross-model transferability. Given that SAUPs impose even more stringent spatial constraints, we also do not observe transferability of SAUPs across the three MLLMs considered in this study.

Robustness and Physical Application. Although we demonstrate the feasibility of hijacking the decision chain via one perturbation, applying such a perturbation to the physical environment remains a significant challenge. The robustness of these perturbations to physical factors, such as lighting conditions and motion blur, requires further study.